ANALYSIS OF ATMOSPHERIC WATER VAPOR MAPS FROM AVIRIS AT SALTON SEA, CALIFORNIA: PART I, EXPERIMENTS, METHODS, RESULTS, AND ERROR BUDGETS

Veronique Carrere, James E. Conel, Robert Green, Carol Bruegge, Jack Margolis, and Ron Alley

Jet Propulsion Laboratory
California Institute of Technology
Pasadena, California

ABSTRACT

AVIRIS data at Salton Sea were processed to yield atmospheric path precipitable water using an algorithm formed from band radiances in and adjacent to near-infrared water vapor absorption bands at wavelengths of 940 and 1130 nm. The retrieval algorithm is termed continuum interpolated band ratio (CIBR). The CIBR is formed as a ratio between an estimated continuum radiance at the absorption band center derived by linear interpolation between out-of-band continuum radiances to either side, and the actual absorption band radiance at the wavelength of maximum absorption. The CIBRs are calibrated for water abundance using the LOWTRAN 7 radiative transfer code and groundbased estimates of visibility obtained at the time of overflight. The CIBR method is easy to implement and computationally rapid in applications to AVIRIS data.

AVIRIS data over the test site were obtained around the time of solar transit in two nearly orthogonal flight lines trending NW and NE and spanning the sea and adjacent land areas. We sought to observe water vapor plume effects from the sea arising from sea-breeze conditions, as well as water emissions from cooling towers of geothermal plants near the southern seashore as means of measuring evaporation phenomena described by the theory of atmospheric diffusion. The occurrence of proximate cultivated and fallow agricultural areas in Imperial Valley underlying one line was also exploited to study possible interference of liquid water bands in vegetation on the CIBR atmospheric water vapor retrievals.

The AVIRIS-generated water maps for Imperial Valley agricultural areas show substantial variations in atmospheric moisture from place to place that appear unrelated to the background of vegetated and unvegetated fields. The column abundances retrieved using the 1130 nm band are in general 50% less than those obtained using the 940 nm band, but the spatial patterns are closely similar. Radiance measurements over the water are used to estimate the random plus coherent noise present in the AVIRIS data. These determinations with error analyses suggest precision of the measurements of about 10% or less. The differences in retrieved amounts between bands are examined from the standpoint of systematic radiometric calibration errors. The discrepancies can arise if the assumed laboratory detector responsivities are about 10% greater than those prevailing in flight. Both the choice of scattering model (e.g., rural vs marine aerosol) and departures from the assumed atmospheric visibility may contribute to uncertainties in the water retrievals.

INTRODUCTION

Atmospheric water vapor is an important reservoir in the global hydrosphere. Water vapor plays a major role in the energetics of the Earth's surface, since on the average almost half of the net local energy transport from surface to atmosphere is by evaporation of water. Water vapor has an important role in the energetics of weather and the general circulation through transport of latent heat by atmospheric motions. Water vapor is an important greenhouse gas. In addition to these major roles in global weather and climate, water vapor band and continuum absorptions provide substantial obstacles to remote sensing of the Earth's surface, especially under clear-air conditions where most surface and atmospheric sounding techniques have their greatest effectiveness. Accurate determination of the abundance and spatial variability of water vapor is therefore important for the understanding of fundamental hydrologic questions and when compensating for atmospheric effects in determination of surface properties.

We report here validation experiments on recoveries of absolute column abundances of water vapor with AVIRIS, together with new mapping applications at 20-m spatial resolution, of path precipitable water over test sites at Salton Sea, California. The validation experiments compare the water abundances retrieved by AVIRIS with abundances derived by ground-based spectroscopic techniques according to the water vapor band models incorporated in LOWTRAN 7, as well as retrievals from single spectral lines, obtained with the high-spectral-resolution Mark IV interferometer. These validation experiments also demonstrate the difficulties attending comparisons between AVIRIS and column abundances derived from radiosondes, thus emphasizing the importance of dependable radiometric calibration of the AVIRIS. The mapping experiments with AVIRIS over this test site have diverse goals, including (1) investigation of surface reflectance (background) interference on column abundance retrieval; (2) comparisons of water abundances derived from different atmospheric water bands, e.g., the 940- and 1130-nm bands, which are influenced by atmospheric scattering, background effects, and instrument calibration; (3) searches for water plume effects from geothermal power facilities as means of studying relationships between moisture source strength and distributed water abundance, as well as water vapor dispersion in the atmospheric boundary layer; (4) study from AVIRIS-derived water maps of the possible mathematical form of boundary conditions on moisture flux under steady winds near the change in surface conditions between the evaporating Salton Sea water body and adjacent dry, sparsely vegetated inland areas; (5) influences of (gentle) topographic effects on moisture distribution; and (6) the analysis of errors in the water recoveries arising from Gaussian electronic and coherent noise present in the AVIRIS data.

SALTON SEA TEST SITE

The Salton Sea is located in the Salton Trough of southeastern California, approximately 240 km (150 miles) ESE of Los Angeles (Figure 1/Slide 8). The water body is roughly 1090 km^2 (420 mi^2) in area, with a present (stable) surface elevation of − 69.1 m (− 226.6 feet) and a maximum depth near 15 m (50 feet). The salinity is about 44,000 ppm, or 1.26 that

of ocean water. The Coachella and Imperial Valleys to the northwest and southeast in the Salton Trough (Figure 1) are well-known areas of intense agricultural activity. Six geothermal power facilities have been developed close to the southeastern shore.

EXPERIMENTAL PLAN EMPLOYING THE OVERFLIGHT PATTERN

On April 18, 1989, between approximately 10:50 and 11:05 a.m. Pacific Standard Time (1900 UT), AVIRIS overflew the Salton Trough along two flight lines oriented at nearly right angles to one another (Figure 1): (1) the first is 57 km in length and oriented N45E; (2) the second is 60 km long and oriented N40W. The two lines overlap in an approximately 11x11 km square area near the northwest end of line 2, mostly over the water. This configuration of flight lines was chosen to support the following experimental goals: (1) Flight line 1 traverses the water body and adjacent sparsely vegetated land areas to the northeast and southwest. We hoped for favorable on-shore wind conditions from sea breezes to investigate changes in atmospheric water vapor distribution across the land-water interface. Depending on the detailed nature of the boundary conditions assumed, we expected to see characteristic changes in both seaward and landward profiles of column abundances of moisture (see Conel, *et al.*, 1988; Brutsaert, 1982; Yeh and Brutsaert, 1971). Attempting to capitalize on often hazy atmospheric conditions in the Salton Trough, the spectral and brightness contrasts between land and water areas were expected to exhibit the so-called adjacency phenomenon arising from atmospheric scattering (e.g., Diner and Martonchik, 1985).(†) (2) Flight line 2 covered an intensely cultivated portion of the northwest Imperial Valley, presenting a checkerboard pattern of vegetated and unvegetated fields which were expected to generate background interference for the water vapor recovery algorithms employed, and possibly local abrupt changes in water column abundance from changes in evapotranspiration and soil moisture evaporation from place to place.

We expected to be able to identify water plumes from cooling evaporators and flash towers at the geothermal plants, to map the associated water distributions, possibly to relate them to theoretical models of atmospheric dispersion from approximately point sources, to compute the anomalous abundances, and to relate these to known strengths of source evaporation for the plants. Finally, we wanted to utilize the crossing portions of the two flight lines to employ water vapor distributions as tracers (Reiter, 1972), to map a kind of convective horizontal velocity-column weighted average or bulk convective velocity and relate it to near surface wind velocity determined with portable meteorological stations.

(†) The sharp contrast in surface reflectance at the shoreline between water and surface vegetation or soil cover plus moderately heavy aerosol loading was expected to generate measurable atmospheric spectral scattering effects over the water. These favorable experimental circumstances were unfortunately compromised by heavy sediment turbidity in the near shore waters, thus drastically reducing the anticipated reflectance contrast and generating considerable inhomogeneity in the water body. The AVIRIS data have consequently not been analyzed further for these effects. These atmospheric scattering experiments will be repeated at a later time, employing a different experimental arrangement together with field observations.

This paper (Part I) describes progress to date on analysis of these experimental goals employing AVIRIS data from the April 18, 1989 overflight of the Salton Sea test site. Part II describes possible applications of the water vapor imagery to several questions of importance for hydrology.

FIELD MEASUREMENTS

During the morning of the overflight and throughout the overflight period itself, ground stations were occupied to measure atmospheric optical depth using a Reagan solar photometer, the line-of-sight column abundance of water vapor with spectral hygrometers, and surface wind direction, wind speed, and atmospheric temperature with mechanical weather stations (Meteorological Research Incorporated Model 1081). The locations of these stations are shown in Figure 1.

Atmospheric optical depth. The Reagan solar photometer provides solar radiance measurements using filters at 10 wavelengths in 10-nm increments between 370 and 1030 nm. The instrument and methods of deriving optical depth via the Langley technique, both as averages over time and on an instantaneous basis, are described by Bruegge *et al.*,(1990) and in earlier references given in that paper. A single solar photometer was available to support the AVIRIS overflight on April 18, 1989. The Langley plot data and optical depths derived therefrom for that date at the western shore station are given in Figure 2. Utilizing the average 550-nm optical depth value, a visibility of 36 km was estimated from formulas given by Elterman (1970) (see Bruegge, 1985) and used to fix the aerosol loading for constraint of the scattering part of the LOWTRAN 7 (Kneizys *et al.*, 1990) radiative transfer model.

Water vapor column abundances. We made measurements of the column abundance of atmospheric water vapor at three locations on the east, west, and southwest shores of the sea, using the Reagan solar photometer 940-nm water channel, and two so-called spectral hygrometers that provide a ratio of radiances in two 10-nm channels at 880 and 935 nm. The column water abundance was derived from the aerosol-corrected radiance at 940 nm via the LOWTRAN 7 atmospheric model (Bruegge, *et al.*, 1990). The spectral hygrometers were originally calibrated using radiosonde data. The hygrometers have been recalibrated, adopting a spectroscopic scale provided by LOWTRAN 7 and using the Reagan photometer as a proxy calibration instrument. This procedure avoids problems inherent in the use of radiosonde data for calibration purposes. These questions are discussed by Bruegge, *et al.*, 1990.

Figure 3 shows the time variation of water column abundance for the LOWTRAN-7-based determinations via the Reagan sunphotometer 940-nm radiance measurement at the three Salton Sea ground stations, rectified to a vertical path.

Wind direction and speed. Using the MRI portable meteorological stations, we acquired continuous wind speed and direction measurements at sites on the western and eastern seashores; at the southern site no such instrumentation was available. Wind direction was measured approximately with a Brunton compass; speed was estimated by walking parallel to the measured direction at the perceived velocity. Winds were steady in magnitude and direction at the northern sites; calm conditions prevailed at

the southern location. The data at times of AVIRIS overflight are shown vectorially in Figure 4.

Ground measurements of surface spectral reflectance. Directional hemispherical spectral reflectance was determined over four unvegetated bright and dark targets (Figure 1) using the Portable Instantaneous Display and Analysis Spectrometer (PIDAS). We plan to use these data for in-flight radiometric calibration of AVIRIS (Green, *et al.*, 1990) and to determine surface spectral reflectance of other targets using an empirical method relating surface reflectance to scanner response (Conel, 1990; Conel, *et al.*, 1989).

ALGORITHM FOR ATMOSPHERIC WATER VAPOR RETRIEVAL

We have employed a computationally simple algorithm (Green, *et al.*, 1990), based on use of the short-wavelength infrared 940-nm and 1130-nm atmospheric water vapor absorption bands, to retrieve atmospheric moisture over land areas. Retrievals over water bodies, where the surface reflectance is zero at these wavelengths will require use of the atmospheric path radiance. The algorithm uses radiance measurements from AVIRIS at the center of an absorption band, together with values of the "continuum" radiances to either side (Figure 5). A value of the continuum radiance at the wavelength of maximum band absorption is estimated by linear interpolation between these adjacent continuum values. A ratio is formed between the interpolated continuum and band radiances, called the continuum interpolated band ratio (CIBR).

It has the form

$$\text{CIBR} = y = L_3/(C_1 L_1 + C_2 L_2) \qquad (1)$$

where C_1 and C_2 are constants, equal to 0.5 at 940 nm, where the measurement channels are equally spaced in wavelength, and 0.52 and 0.48 respectively for 1130 nm, where they are unequally spaced. To provide a calibration relationship between the CIBR as defined in Equation 1, and column water abundance w, measured in g H_2O/cm^2, we employed the LOWTRAN 7 radiative transfer code with the following conditions: (1) midlatitude summer; (2) surface elevation = sea level; (3) default rural aerosol model (Detailed descriptions of the aerosol scattering phase functions utilized in LOWTRAN are given by Kneizys, *et al.* (1983).); (4) 36-km visibility; (5) surface (Lambertian) spectral reflectance = 0.25; (6) altitude of AVIRIS observation = 20 km, (7) latitude = 33.2°N longitude = 115.50°W, (8) solar zenith angle = 24.9°. The resulting calibration curves are shown in Figure 6. These have the convenient and accurate functional forms

$$y = \exp(-\alpha w^{\beta}) \qquad (2)$$

where α and β are constants. This algorithm is sensitive to the presence of water absorption bands in the surface reflectance that arise from vegetation (Figure 7), since the surface and atmospheric bands overlap one another. Accordingly, under some conditions, extraction of the surface band

contribution from the total water present will require assumption of a band model for the surface part, since the observed radiance (one observation) at wavelengths within the atmospheric band consists of contributions from both atmosphere and surface. For conditions of low visibility (e.g., a few tens of km), the algorithm is sensitive to the visibility and to the aerosol model employed. The uncertainties introduced by each of these problems are discussed below.

WATER VAPOR MAPS OVER THE NORTHWEST IMPERIAL VALLEY

Figure 8a/Slide 9 shows a three-color composite image of AVIRIS data from one segment of the northwest-southeast trending flight line. The lattice pattern of field boundaries is laid out along section lines, north being down and to the left, east up and to the left. The distance between geothermal plants U2 and U3, depicted by x's, is 0.5 mile (0.8 km). The distribution of vegetated, partially vegetated, and fallow agricultural areas for April 18, 1989 are shown in shades of green in Figure 8a. The column abundance distribution of atmospheric water vapor, calculated from the 940-nm water band, is shown in Figure 8b. These values have been rectified to a vertical path assuming local atmospheric homogeniety. It is readily apparent that superposed upon regional trending bands of variable moisture is a "residual" pattern of the fields. In Figure 9/Slide 10, the green field pattern from Figure 8b/Slide 9 has been superposed on the water image to facilitate a closer comparison. In general, there appears to be no correlation between the distribution of green fields and the total column abundance of water present. That is, the presence of green vegetation at the surface does not appear to enhance the atmospheric moisture component at the level of water vapor subdivision depicted. Nor does the presence of an unvegetated substrate generate any systematic pattern of retrieved abundance relative to the surroundings. However, the vegetation must influence the retrieved abundances. This problem is dealt with below.

COMPARISON OF RETRIEVALS FROM THE 940- AND 1130-NM BANDS

In Figure 10/Slide 11 we present a comparison of water abundances retrieved from the CIBR algorithms for the 940- and 1130-nm bands, represented on a common color scale. While the overall pattern of retrieved moisture is very similar, the derived water abundance for 1130 nm is systematically lower than that for 940 nm everywhere in the image. A similar discrepancy was found for retrievals at Salton City (Figure 2).

VALIDATION EXPERIMENTS AND PRECISION OF THE WATER VAPOR RETRIEVALS

Validation via LOWTRAN 7 and single spectral line determinations. Good agreement has been found between column abundances derived from AVIRIS, when the instrument has been calibrated in flight, and abundances measured simultaneously from the ground with the Reagan solar photometer (Bruegge, *et al.*, 1990). Bruegge, *et al.* (1990) have further compared the column abundances derived from the solar photometer data based on LOWTRAN 7 with column abundances derived from analysis of eight mid-infrared single-line profile measurements obtained with a high-spectral-resolution interferometer (JPL Mark IV). The scatter of the eight interferometer determinations is ±3%; the agreement between the LOWTRAN 7-based solar photometer retrievals and the single-line determinations is about 1%.

Estimating precision of determinations. Close inspection of the images of Figure 8 shows the presence of a grainy pattern over the water and elsewhere that represents both coherent and random electronic noise components. A coherent noise component with a frequency near 400 Hz is known in the AVIRIS data and has been traced to a power supply aboard the ER-2 aircraft. Random electronic noise, represented by dark current fluctuations measured at the end of each AVIRIS scan line, is present at the level of about ±3 DN, equal to a noise equivalent radiance of about 0.1 $\mu W/(cm^2\ sr\ nm)$ (Chrien, *et al.*, 1990)

The fractional uncertainty in the CIBR (= y) σ_y/y is derived from Equation 1 as

$$\sigma_y/y = \sqrt{(y^2 C_1 \sigma_1^2 + C_2^2 \sigma_2^2 + C_1 C_2 \sigma_{12}^2} \qquad (3)$$

$$- 2yC_1\sigma_{13}^2 - 2C_2\sigma_{23}^2 + \sigma_3^2)/L_3$$

where σ_j and σ_{ij} are diagonal and off-diagonal elements of the covariance matrix of the L_j, obtained from analysis of the radiances observed by AVIRIS over the water. σ_j and σ_{ij} contain components arising from both coherent and random noise plus possible variations in the atmospheric path radiance over the areas sampled. Also included are possible contributions from variability of the water surface, wherever the reflectance is nonzero because of suspended sediment or organic load. For the Salton Sea data of April 18, 1989, the variance-covariance matrix in terms of the radiances (× 100) derived from analysis of 2500 pixels over the water is

$$\begin{bmatrix} \sigma_1^2 & & \\ \sigma_{12}^2 & \sigma_2^2 & \\ \sigma_{13}^2 & \sigma_{23}^2 & \sigma_3^2 \end{bmatrix} = \begin{bmatrix} 63.1 & & \\ 7.3 & 20.3 & \\ -7.9 & -3.6 & 25.7 \end{bmatrix}$$

for the 940-nm band, and

$$\begin{bmatrix} 33.82 & & \\ -4.3 & 40.0 & \\ 5.8 & -5.4 & 30.8 \end{bmatrix}$$

for the 1130-nm band. The fractional uncertainties in derived precipitable water values are, from Equation 2,

$$\sigma_w/w = (\sigma_y/y)/(\alpha\beta w^{\beta}) \qquad (4)$$

Values of σ_w/w (in percent) that result from these variance-covariance data are shown in Figure 11 for four areas within the AVIRIS data segment under discussion. The values of σ_y/y for the 1130-nm band correspond closely to the values shown for σ_w/w and are not included for clarity. The notation $\sigma_{ij}^2 = 0$ corresponds to an uncertainty estimate excluding the covariances. In general, the uncertainty increases slighly when the covariances are included in the error budget, but in all cases the retrievals appear to be good to better than 10% for the present data set.

SOME SOURCES OF SYSTEMATIC ERROR

Systematic errors manifest themselves as differences in water abundances derived from the 940- and 1130-nm water bands (Figures 3, 10 and 11) amounting to about 55%. Such errors may arise from any or all of the following: (1) spectral dependence of the surface reflectance violating the constant-with-wavelength assumption, (2) calibration errors, (3) departures of the actual atmospheric visibility from that assumed in constructing the calibration curves (Equation 2) from LOWTRAN 7, (4) an incorrect assumption of the aerosol model in LOWTRAN 7 as compared to the actual conditions, or (5) incompleteness one or both of the band models employed in LOWTRAN 7. Items 1 thru 4 are discussed below. Item 5 cannot be evaluated from the AVIRIS data themselves.

Spectrally dependent background reflectance. The spectral reflectance of the Earth's surface is seldom constant with wavelength. Properly, the calibration relationship between CIBR and water abundance needs to be generated with the actual surface spectral reflectance over which the water retrieval is to be carried out. In practice this is difficult because the a priori surface reflectance is not known, so an iterative scheme has to be developed to estimate it.

The CIBR calibration curves given in Figure 6 are calculated from LOWTRAN 7 on the assumption of a constant surface spectral reflectance of 25%. We will refer to this as the standard curve. In this section we describe calculations using the LOWTRAN 7 model that explore departures from this assumption. Surface reflectance effects that are not included in the standard calibration curve introduce a systematic error into the retrieved water abundances. The magnitude of these is investigated next.

We reevaluated the CIBR calibration functions (Equation 2) employing LOWTRAN7 with the spectral reflectance of alfalfa, iron-oxide-rich soil, and the mineral gypsum as representative of possible extreme natural examples introduced by background reflectance. The reflectance data obtained with a laboratory spectrometer are shown in Figure 7. The fractional differences $(y_s - y)/y_s$ in water vapor retrieved using the standard CIBR calibration curve (y_s) and the wavalength-dependent CIBR curves (y) for these cases are given in Figure 12. The wavelength-dependent calibration functions follow from these, given the standard curve. The background reflectance changes introduce small changes in the constants α_s and β_s, $\Delta\alpha$, and $\Delta\beta$. The corresponding change in y_s is approximately

$$\Delta y_s \cong \left(\frac{\partial y_s}{\partial \alpha_s}\right)\Delta\alpha + \left(\frac{\partial y_s}{\partial \beta_s}\right)\Delta\beta \qquad (5)$$

The accompanying fractional uncertainty in the water vapor recovery is

$$\frac{\Delta w}{w} \cong -\left(\frac{\Delta y_s}{y_s}\right)\frac{1}{\alpha_s \beta_s w^{\beta_s}} \qquad (6)$$

or written out, using Equation 2

$$\frac{\Delta w}{w} \cong \frac{1}{\beta_s}\left(\frac{\Delta\alpha}{\alpha_s}\right) + \ln(w)\left(\frac{\Delta\beta}{\beta_s}\right) \qquad (7)$$

The values of $\Delta\alpha/\alpha_s$ and $\Delta\beta_s/\beta$ derived from the data of Figure 12 and the standard calibration equation are listed in Table 1 for alfalfa and iron-oxide-rich soil. The case of gypsum-rich soil closely resembles that of alfalfa and is therefore not presented.

Table 1. Fractional (systematic) changes (%) in the constants α and β of Equation 2 accompanying departures of the surface reflectance from 0.25

	$\Delta\alpha/\alpha_s$	$\Delta\beta/\beta_s$
Alfalfa	2.37	2.07
Fe_2O_3 soil	2.87	−1.79

The fractional (systematic) errors in water recovery implied by Equation 7 for iron-oxide-rich soil and alfalfa backgrounds are shown in Figure 13. The most extreme case is that of low atmospheric water abundance (< 0.5 cm), where it is seen that the errors grow without bound as w approaches zero. The presence of surface absorption bands increases the apparent water abundance retrieved for both cases, as expected. For typical abundances present in the Salton Sea data set (~ 1.5 to 2 g/cm^2), the reported amounts would be about 5% too high for both vegetation and soil backgrounds.

Radiometric calibration uncertainty. The in-flight radiometric calibration of AVIRIS is uncertain because of changes in spectrometer configuration that may accompany (possibly time-dependent) thermal distortion of the instrument away from the steady configuration under which the laboratory calibration is carried out. These (distortion) changes introduce a systematic error Δy into the calculated *CIBR* values that is given by

$$\Delta y = y\{\delta L_3 - y(C_1\delta L_1 + C_2\delta L_2)/L_3 \qquad (8)$$

where the δL_j represent changes in the L_j arising from the supposed distortion. If Φ_j represents the proportionality constant between radiance and instrument output in DN for the jth channel involved in the

CIBR calculation, e.g., $L_j = \Phi_j^{-1} DN_j$, (j = 1,2,3), then $\delta L_j = L_j' - L_j = (\Phi_j'/\Phi_j - 1)L_j$, where the primes refer to flight conditions. It has not yet been possible to provide an in-flight calibration for AVIRIS from the ground-based data for the Salton Sea experiment of April 18, 1989. We can, however, estimate in-flight changes in the Φ_j that will account completely for the discrepancies, as follows. In Figure 14 the AVIRIS-derived column abundances for western and southern observation stations are compared with time histories of variation of the atmospheric water derived from analysis of Reagan sun photometer and spectral hygrometer data. Assuming the ground-based observations of water vapor abundance to be correct, the AVIRIS abundances are between 18-22% too low at 940 nm, and 46-58% low at 1130 nm. The required changes in in-flight gain factors are illustrated in Figure 11, as derived from Equations 2 and 5. To reduce the number of variables, the second term on the right-hand side of Equation 5, involving both δL_1 and δL_2, has been treated as a single algebraic variable. Specifically, at 940 nm, a discrepancy $\delta w/w$ of − 20% could arise from a +8% change in δL_3 together with ≈ − 9% in the algebraic value of $\delta L_1 + \delta L_2$. Lacking other constraints, any combination of the δL_j satisfying Equation 5 would be equally acceptable. The magnitude of these changes are in accord with those found from available analyses of in-flight AVIRIS detector responsivities (Green, *et al.*, 1990). At 1130 nm, the greater magnitude of $\delta w/w$ implies greater differences between laboratory and flight conditions than in the 940-nm region, although uncertainty in the laboratory responsivities may also be involved at 1130 nm.

Atmospheric visibility. The water calibration functions (Equation 2) depicted in Figure 5 were developed from LOWTRAN 7 under the assumptions of uniform surface reflectance of 0.25, constant visibility of 36 km, and the standard rural aerosol model contained in the LOWTRAN 7 code. Dependence of the apparent retrieved water abundance upon departures of the actual visibility from the assumed value, and upon the aerosol model assumed, are illustrated in Figure 15, where results for the rural and maritime models are compared. In either case, if the actual visibility encountered is greater than 36 km (crossover point of equal water retrieval for both bands in both scattering models), the radiances generated by LOWTRAN 7 provide lower than expected abundances for both 1130- and 940-nm retrievals with $w_{1130} > w_{940}$ by about 9%. With visibilities less than 36 km, the retrieved abundances are greater than expected, and $w_{940} > w_{1130}$. The maritime model generates higher apparent precipitable water abundances than does the rural model for visibility less than the assumed standard value, and less apparent water for visibilities that are greater than 36 km.

Rural vs maritime aerosol models. If the radiances as a function of visibility are calculated assuming a marine aerosol model in LOWTRAN 7, but the rural aerosol-based calibration curve for water vapor column abundance recovery is erroneously retained, the crossover point shifts to a visibility of 50 km, and the apparent retrieved water amounts are increased. For large visibilities the water amounts converge to the same values for each band, independent of the scattering model, as would be expected for zero scattering conditions. The difference in indicated amount between bands is about 9%.

To explain a condition of $w_{940} > w_{1130}$ retrieved from the AVIRIS observations at Salton Sea, based on assumptions about the aerosols, requires a visibility less than 36 km everywhere if either the rural or

maritime model is adopted. This includes the west shore calibration site, where the visibility estimate was established from our sun photometer data, and consequently where the two band estimates should agree. A 50% discrepancy, based on visibility or scattering model, violates the observed visibility condition and would also produce larger moisture amounts (e.g., >> 2 cm) than are observed over the site.

The differences in apparent water vapor amount between the rural and maritime aerosol models shown in Figure 16 suggest that the crossover water abundance for the adopted visibility may depend upon the scattering model used. This, however, is not the case. The apparent difference results from the use of radiance calculations from one aerosol (maritime) model in a water vapor calibration curve derived from another (rural) model. These differences disappear when the marine model radiances are used in a marine model calibration curve (as shown in Figure 15), although the functional dependence of retrieved water abundance on departure of visibility from the assumed standard value remains.

ACKNOWLEDGMENTS

This paper presents the results of one phase of research carried out at the Jet Propulsion Laboratory, California Institute of Technology, under a contract with the National Aeronautics and Space Administration.

REFERENCES

Bruegge, C.J., 1985, In-flight absolute radiometric calibration of the Landsat Thematic Mapper (published under Kastner), Ph.D. Dissertation, University of Arizona, 195 pp.

Bruegge, C.J., J.E. Conel, J.S. Margolis, R.O. Green, G. Toon, V. Carrere, R.G. Holm, and G. Hoover, 1990, In-situ atmospheric water-vapor retrieval in support of AVIRIS validation, in *Imaging Spectroscopy of the Terrestrial Environment, SPIE Vol. 1298.*

Brutsaert, W., 1982, *Evaporation into the Atmosphere,* D. Reidel Publishing Company, Boston, 299 pp.

Chrien, T.G., R.O. Green, and M.L. Eastwood, 1990, Accuracy of the spectral and radiometric laboratory calibration of the Airborne Visible/Infrared Imaging Spectrometer (AVIRIS), proceedings of this conference (in press).

Conel, J.E., R.O. Green, V. Carrere, J.S. Margolis, G. Vane, C. Bruegge, and R. Alley, 1989, Spectroscopic measurement of atmospheric water vapor and schemes for determination of evaporation from land and water surfaces using the Airborne Visible/Infrared Imaging Spectrometer (AVIRIS), *IGARSS '89, 12th Canadian Symposium on Remote Sensing,* **IEEE #89CH2768-0**, 2658 - 2663.

Conel, J.E., 1990, Determination of surface reflectance and estimates of atmospheric optical depth and single-scattering albedo from Landsat Thematic Mapper data, *Int. J. Remote Sensing,* **11(5)**, 783-828.

Diner, D.J., and J.V. Martonchik, 1985, Influence of Aerosol Scattering on Atmospheric Blurring of Surface Features, *IEEE Transactions on Geoscience and Remote Sensing*, GE-23 (5), 618-624.

Elterman, L., 1970, Vertical-attenuation model with eight surface meteorological ranges 2 to 13 kilometers, Report AFCRL-70-0200, AFCRL, Bedford, MA, 55 pp.

Green, R.O., V. Carrere, and J.E. Conel, 1990, Measurement of atmospheric water vapor using the Airborne Visible/Infrared Imaging Spectrometer, *Image Processing '89*, American Society for Photogrammetry and Remote Sensing, Proceedings of a conference at Sparks, Nevada, 23 May, 1989, 31-44.

Isaacs, R.G., W.-C. Wang, R.D. Worsham, and S. Goldenberg, 1987, Multiple-scattering LOWTRAN and FASCODE models, *Appl. Optics*, 26(7), 1272-1281.

Kneizys, F.X., E.P. Shettle, W.O. Gallery, J.H. Chetwynd, L.W. Abrew, J.E.A. Selby, S.A. Clough, and R.W. Fenn, 1983, Atmospheric Transmittance/Radiance: Computer Code LOWTRAN 6, AFGRL TR-83-0187, AFGL, Hanscom AFB, MA, 193-200.

Kneizys, F.X., E.P. Shettle, G.P. Anderson, L.W. Abrew, J.H. Chetwynd, J.E.A. Shelby, and W.O. Gallery, 1990, Atmospheric Transmittance/Radiance: computer Code LOWTRAN 7, (in press), AFGL Hanscom AFB, MA.

Reiter, E.R., 1971, *Atmospheric Transport Processes (Part 2: Chemical Tracers)*, U.S. Atomic Energy Commission Critical Review Series (TID-25314), 65-94.

Yeh, G.T., and W. Brutsaert, 1971, A solution for simultaneous turbulent heat and vapor transfer between a water surface and the atmosphere, *Boundary-Layer Meterol.*, 2, 64-82.

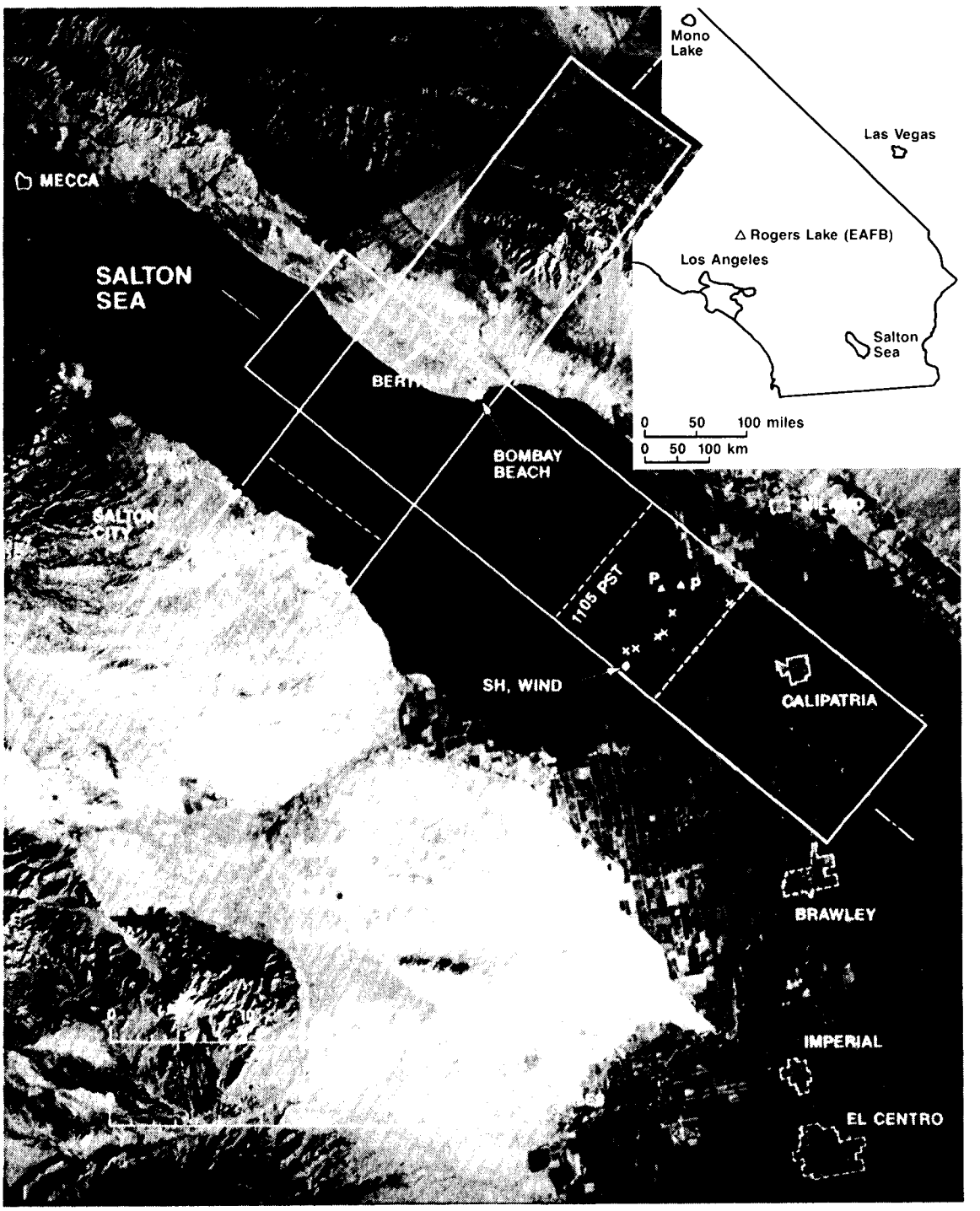

Figure 1. Location of the Salton Sea test site in southeastern California (inset). MSS image shows orientation and extent of the AVIRIS flight paths over Salton Sea, in the Salton Trough, April 18, 1989. Places mentioned in the text but not shown on this index photo include: (1) Imperial Valley - extends southeast from southeast shore of Salton Sea including agricultural areas shown in red (slide only) and the cities of Niland, Calipatria, Brawley, Imperial, and El Centro, (2) Coachella Valley - extends northwest off the image from northwest shore of Salton Sea near the town of Mecca.

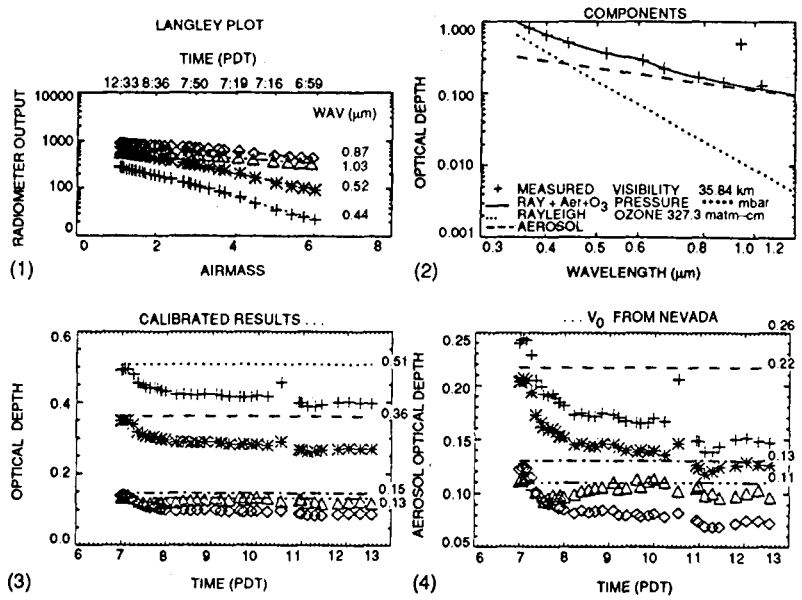

Figure 2. Atmospheric characterization via Reagan sun photometer at Salton City, 18 April 1989. (1) Langley plot - Raw radiometer output versus airmass, 1/cos (solar zenith angle), (2) Components of the optical depth derived from the Langley plot data, (3) Calibrated results - instantaneous optical depths derived from two-point Langley plots using instrument calibration constants (V_0) derived from long-term-average zero-air-mass intercepts, (4) V_0 from Nevada - instantaneous aerosol optical depths derived from two-point Langley plots using V_0 values derived from high-altitude measurements at Charlton Peak, Nevada.

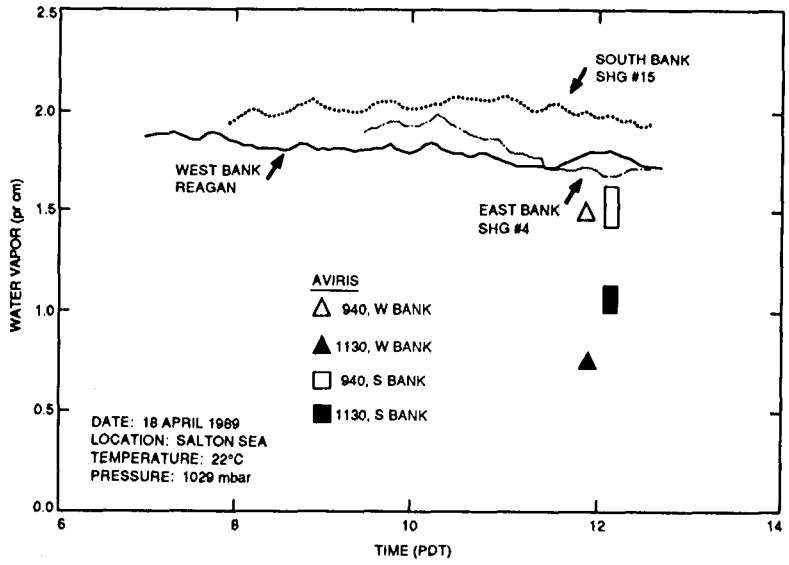

Figure 3. Instantaneous water vapor determinations from ratioing spectral hygrometer and Reagan sun photometer data at Salton City. AVIRIS determinations are via the CIBR method with LOWTRAN 7 code, using laboratory-determined responsivities to calculate inflight radiances. See text for complete explanation.

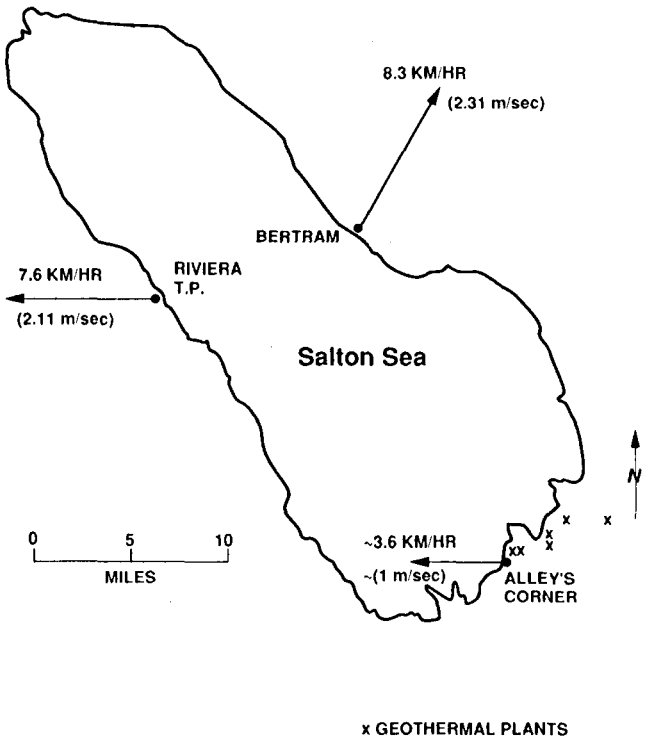

Figure 4. Wind directions and speeds at 2 meters above ground level at time of AVIRIS overpass, as measured by mechanical weather stations.

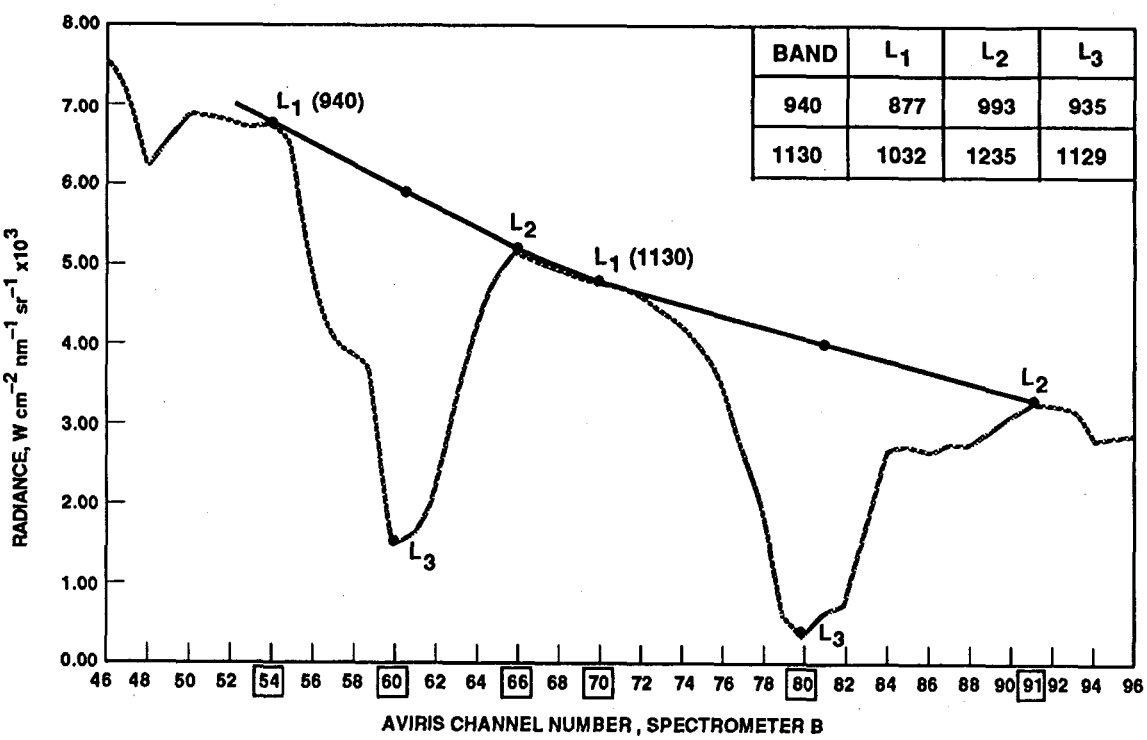

Figure 5. Wavelengths and radiance values used to calculate the *Continuum Interpolated Band Ratio (CIBR)* from AVIRIS radiance data.

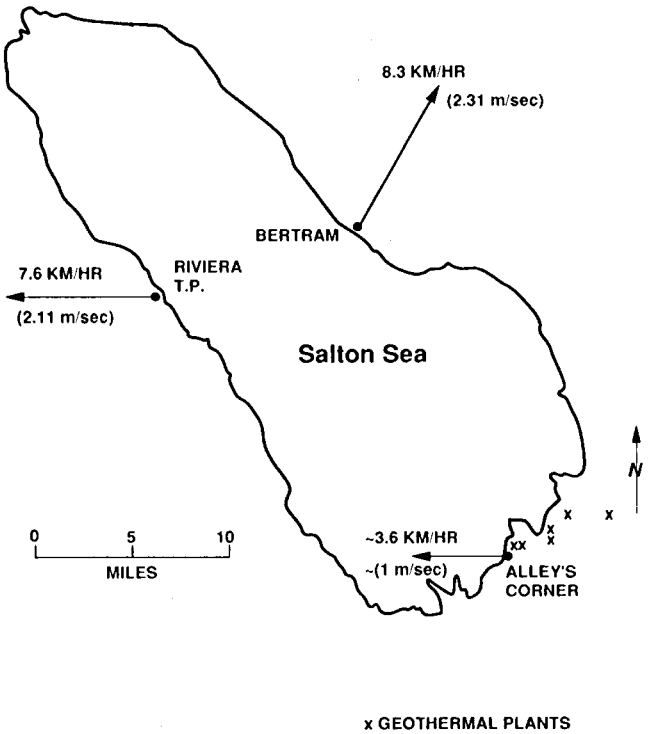

Figure 4. Wind directions and speeds at 2 meters above ground level at time of AVIRIS overpass, as measured by mechanical weather stations.

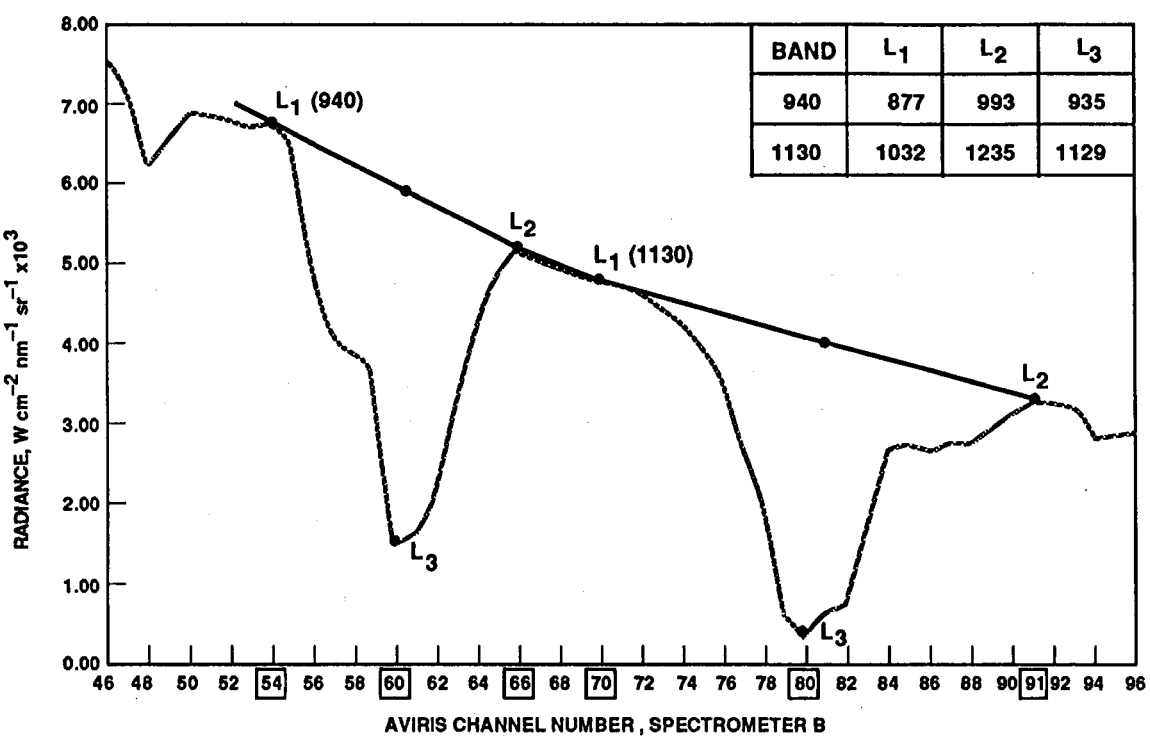

Figure 5. Wavelengths and radiance values used to calculate the *Continuum Interpolated Band Ratio (CIBR)* from AVIRIS radiance data.

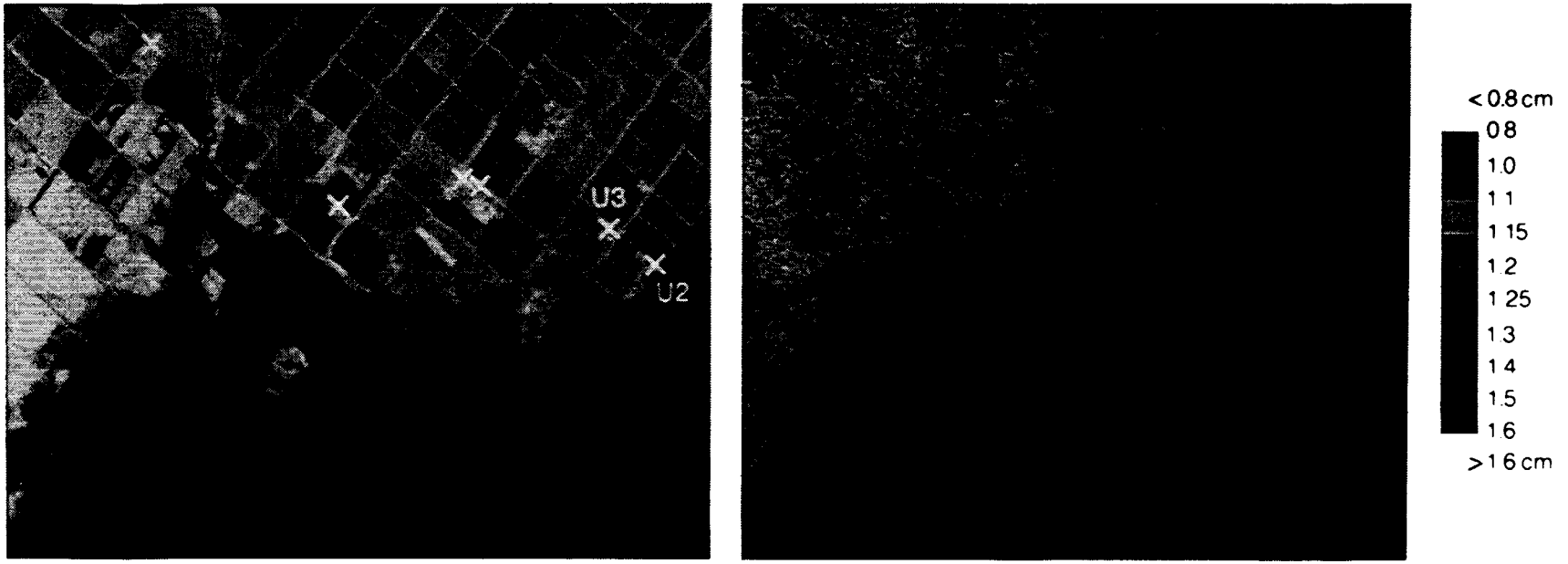

Figure 8. Left image: - three-color composite AVIRIS image of near-shore area (11:05 PST segment) in northwest Imperial Valley. Right image: - spatial distribution of atmospheric water vapor (column abundance) derived using CIBR algorithm and 940-nm water band.

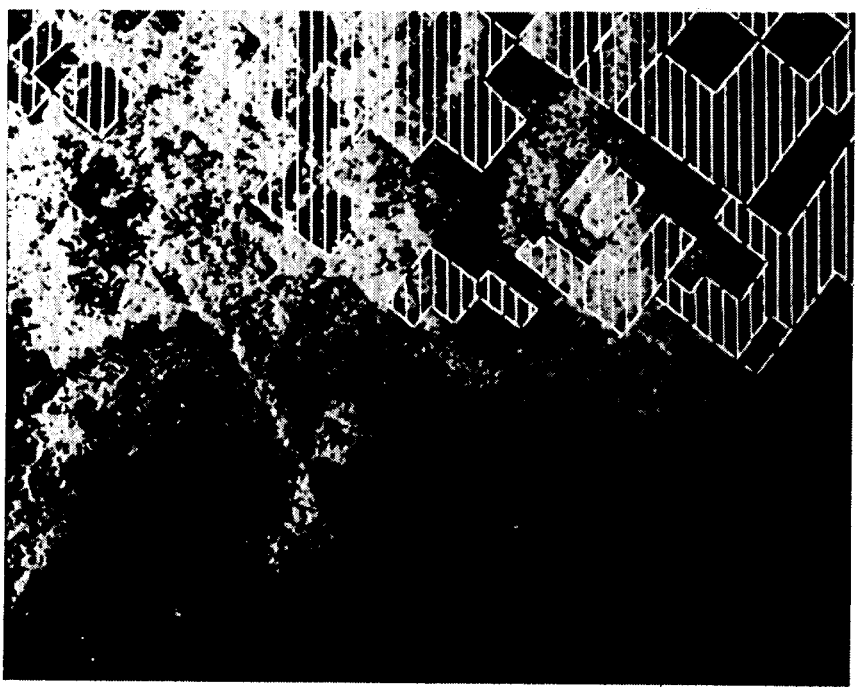

Figure 9. Spatial distribution of atmospheric moisture (column abundance) compared to the distribution of green fields as shown in left image of Figure 8. The *median filter* replaces image DN at a pixel P by the most frequent DN value in the 3x3 array of which P is the center.

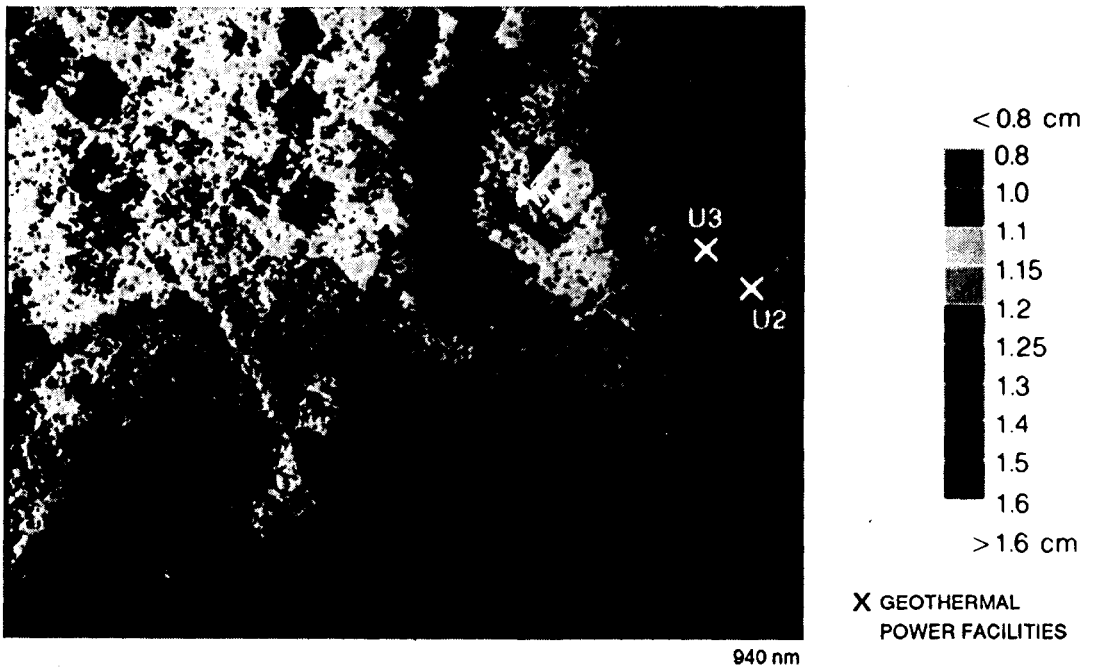

Spatial distribution of water vapor
940 nm Atmospheric water band

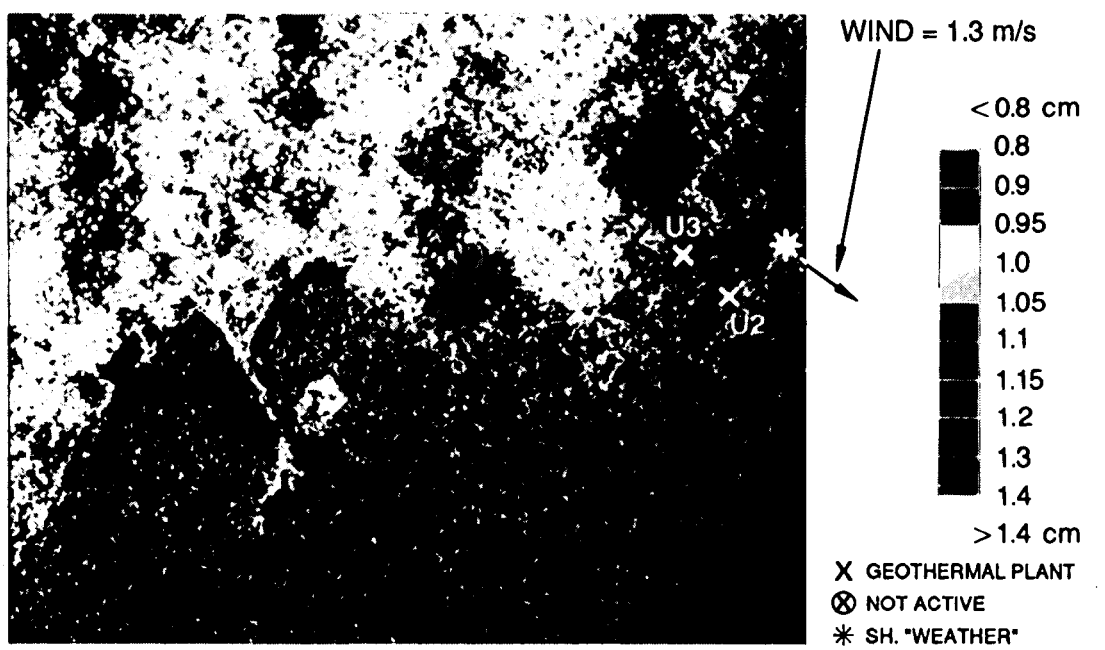

Spatial distribution of water vapor
1130 nm Atmospheric water band
Median Filter

Figure 10. Spatial distribution of atmospheric water vapor (column abundance) derived by the CIBR algorithm for the 940- and 1130-nm water bands. The median filter replaces image DN at a pixel P by the most frequent DN value in the 3×3 array with center at P.

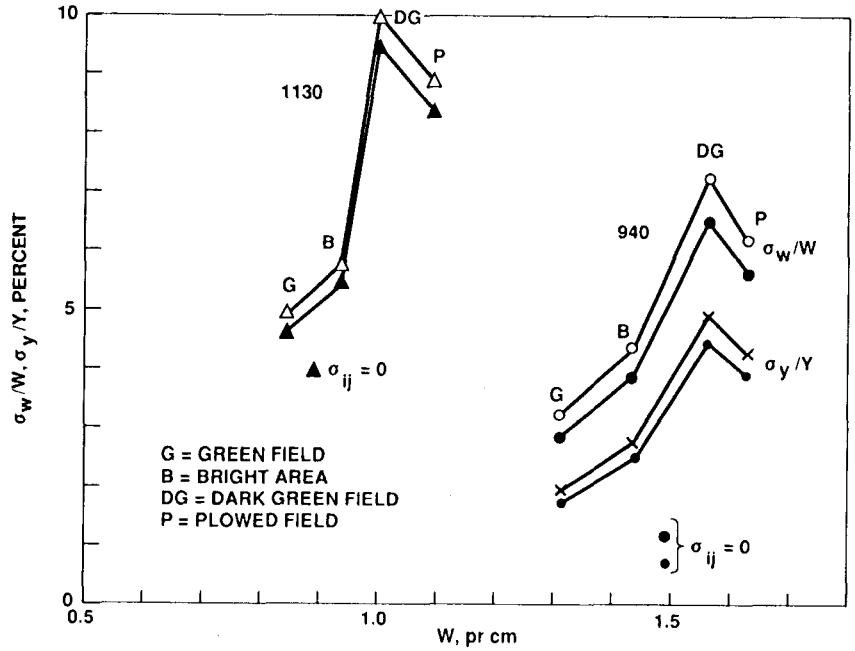

Figure 11. Fractional error in the recovered water abundance for 940- and 1130-nm bands using the CIBR algorithm over selected surface targets. Variances and covariances estimated from radiance data over a 2500-pixel area of Salton Sea northwest of the 12:05 PDT segment of the NW-SE flight line.

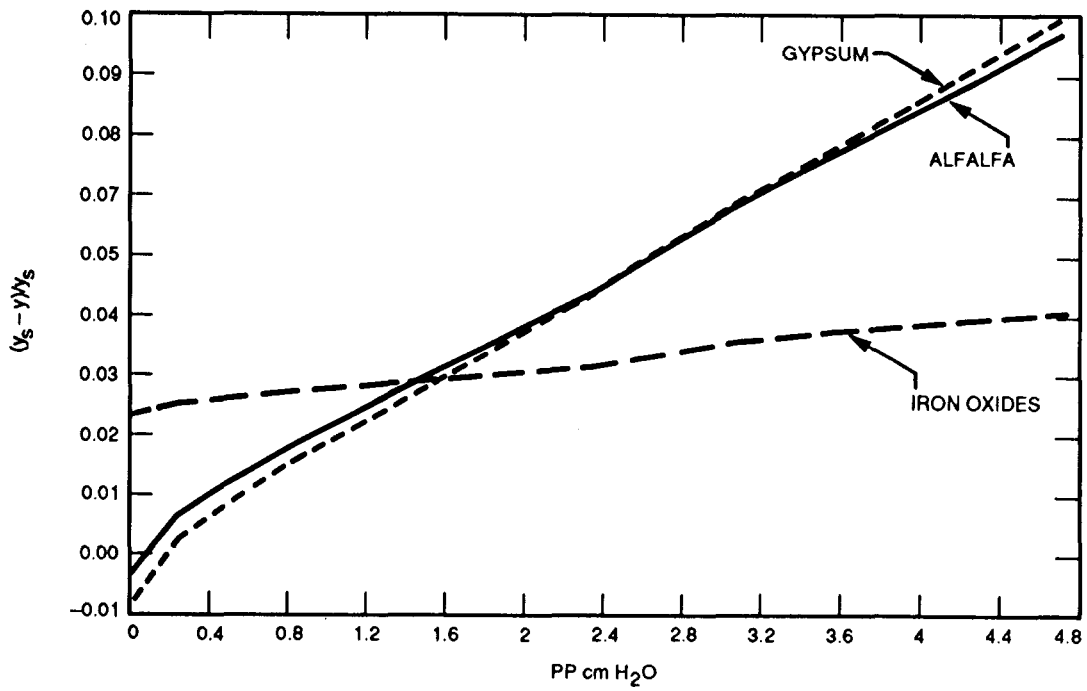

Figure 12. Normalized differences between the standard CIBR derived with constant surface reflectance of 0.25 and CIBR derived with surface reflectances of alfalfa, and iron-oxide- and gypsum-rich soils, calculated as a function of path precipitable water.

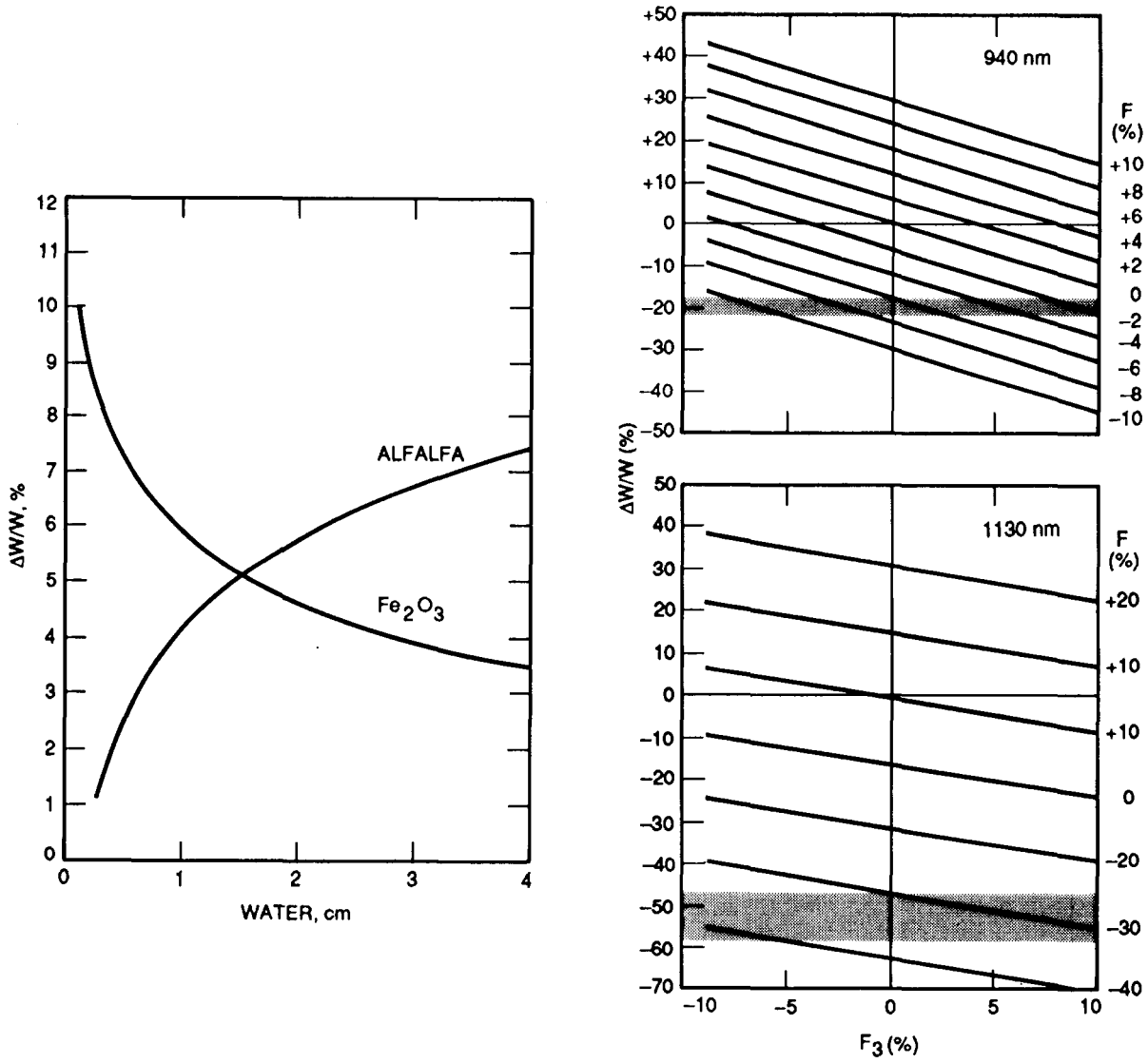

Figure 13. Fractional (systematic) error in percent of water retrieved using the standard CIBR calibration curve for background reflectance of iron- oxide-rich soil and alfalfa.

Figure 14. Fractional (systematic) uncertainty in recovered water vapor abundances for 940- and 1130-nm bands introduced by changes in radiometric calibration of AVIRIS during flight. Water abundance assumed is 1.54 g/cm^2. The variable δL_{12} is equal to $\delta L_1 + \delta L_2$, the combined (algebraic) change in the radiances L_1 and L_2. The horizontal axis F_3 is the percent change in the radiance L_3. The horizontal (shaded) areas depict regions where combinations of radiance changes for L_1, L_2, and L_3 may lie to produce observed discrepancies between ground radiometer-based and AVIRIS-based water retrievals.

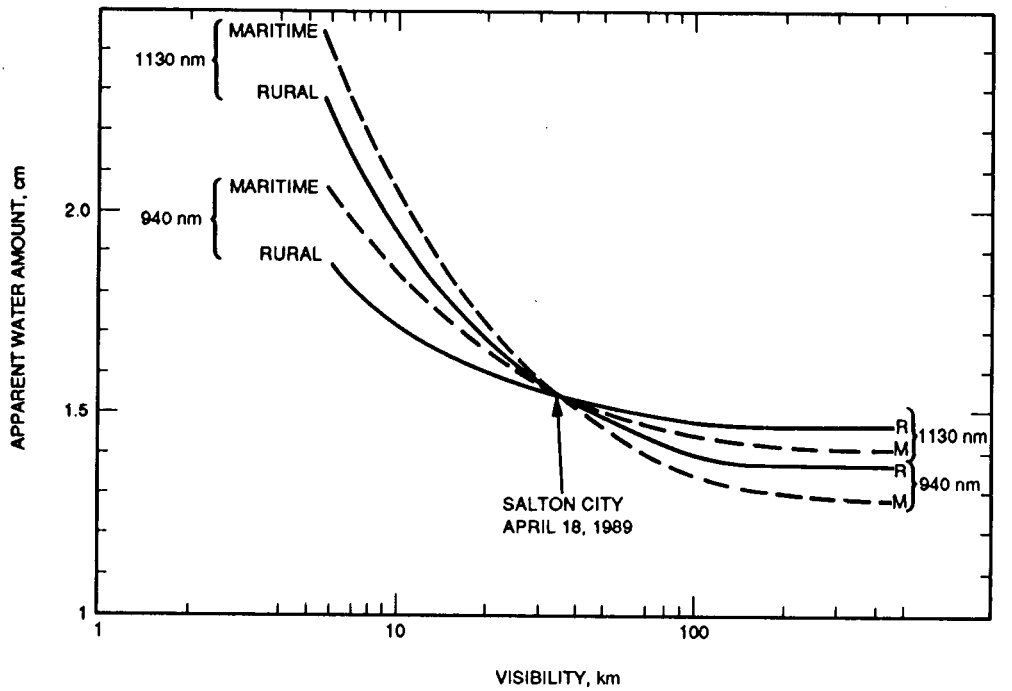

Figure 15. Dependence of apparent retrieved water vapor (column) abundance upon atmospheric visibility, calculated according to LOWTRAN 7 with a rural aerosol model.

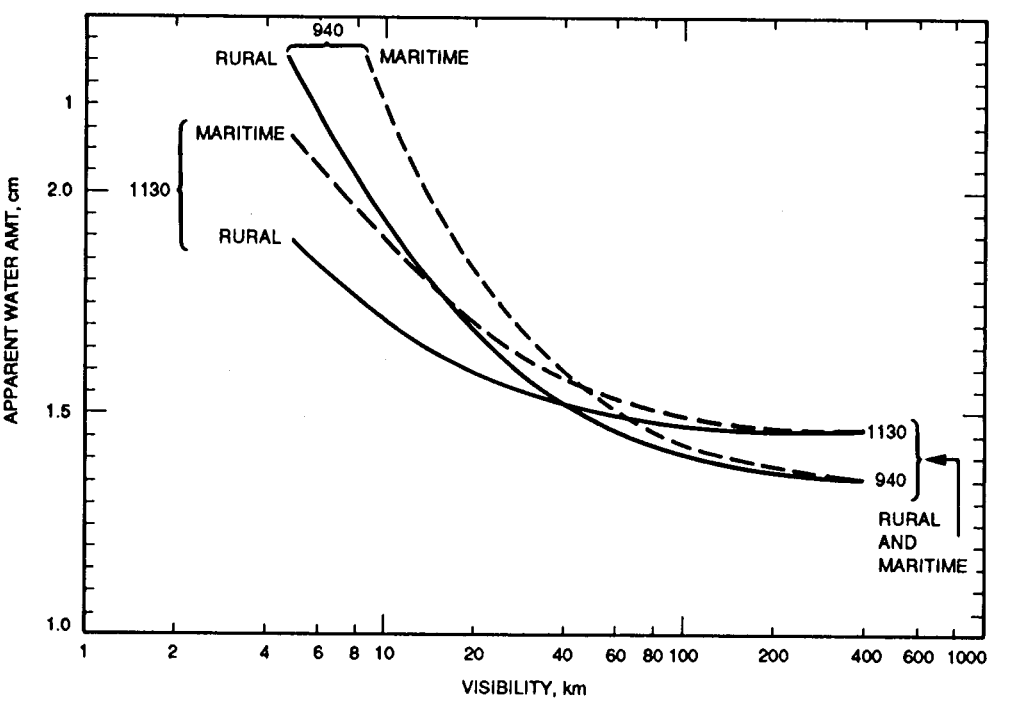

Figure 16. Dependence of apparent retrieved water vapor (column) abundance upon atmospheric visibility and the aerosol model employed, calculated according to LOWTRAN 7. Curves labeled "marine" represent apparent abundances derived from a marine aerosol model but retaining the rural aerosol-based calibration curve.